Integration of Radiative Cooling and Solar Heating in Thermal Management Films for Year-Round Energy Savings

Ruiming Tan,[a] Yinyan Li,[a] Gongxun Bai,*[a] Cuilu Xi,[a] Peng Xue,*[b] Yuxin Ma,[b] Beibei Xu,[c] Shiqing Xu[a] and Jianhua Hao*[d]

[a] *College of Optical and Electronic Technology, China Jiliang University, Hangzhou 310018, P. R. China*. Email: *baigx@cjlu.edu.cn;*

[b] *Beijing Key Laboratory of Green Building Environment and Energy Saving Technology, Beijing University of Technology, Beijing 100124, P. R. China*. Email: *xp@bjut.edu.cn*

[c] *State Key Laboratory of Modern Optical Instrumentation, School of Optical Science and Engineering, Zhejiang University, Hangzhou 310027, P. R. China.*

[d] *Department of Applied Physics, The Hong Kong Polytechnic University, Hong Kong 999077, P. R. China*. Email: *jh.hao@polyu.edu.hk*

ABSTRACT

The application of zero-emission passive radiative coolers is a crucial step towards global carbon neutrality. However, a single radiative cooling function cannot meet the thermal requirements under various weather conditions. We present a dual-mode thermal management film that integrates passive radiative cooling and heating functions through its porous polymer surface for cooling and a light-to-heat conversion surface enabled by graphene and carbon nanotubes for heating. Physically flip the surfaces of the dual-mode film, positioning the corresponding surface toward solar radiation to obtain the desired functionality. In cooling surface, the film achieves subambient cooling of ≈13.3 °C under 853.88 W m^{-2} of sunlight, thanks to its high solar reflectance (0.92) and mid-infrared emissivity (0.95). In heating surface, it uses high solar absorption (0.90) to increase the temperature by 11.4 °C and generates Joule heating at various voltage levels. According to EnergyPlus software estimates, buildings with roofs covered in the film could reduce CO_2 emissions by 1.109 billion metric tons, equivalent to 3% of current global CO_2 emissions. This study offers a promising solution to climate challenges and holds great potential for energy savings and carbon reduction.

KEYWORDS: thermal management, passive radiative cooling, passive solar heating, Joule heating, year-round energy saving

INTRODUCTION

To keep the human body in a comfortable environment, cooling during hot weather and heating during cold weather are indispensable. However, traditional cooling and heating technologies consume large amounts of energy, increase greenhouse gas emissions.[1-4] It has been reported that buildings account for more than 30% of global

energy consumption in 2021,[5-7] of which about 50% is used for heating, ventilation and air conditioning,[7] while greenhouse gases emitted from buildings account for 10% of global greenhouse gas emissions.[8] It is estimated that even a slight decrease of 1 ℃ in temperature can significantly reduce electricity consumption by 3-5%.[9,10] Therefore, building an integrated technology with zero pollution, zero energy cooling and zero energy heating to save energy and achieve carbon neutrality by 2050 is a key part of our journey towards a low-carbon life.[11-15]

Passive daytime radiative cooling (PDRC) technology is one of the zero-energy and promising cooling technologies with practical applications, which can effectively reflect solar thermal radiation (200-2500 nm) without any electric power input. Moreover, the cooler can send the heat to the outer space through the atmospheric transparent window (8-13 μm).[16-20] Therefore, the ideal PDRC should have a high reflectivity between 200 and 2500 nm and a high emissivity in the atmospheric transparent window.[21-23] These designs of PDRC can be divided into multilayer photonic structures,[24-26] aerogel structures,[27-29] and porous structures[30-32] to achieve all-weather passive radiative cooling. Conversely, the green passive solar heating (PSH) technology utilizes ideal heating materials with high absorbance at 200-2500 nm and low emissivity at >2500 nm for efficient heating.[33] Many studies on radiative cooling and heating demonstrate thermal regulation, but they often overlook practical outdoor applications. Without robust self-cleaning functions, performance degrades over time. For instance, Shi et al. used PVDF and MXene for cooling and heating,[34] but the cooling side had hydrophobicity of only 107°, well below the superhydrophobic threshold of 150°. Additionally, the heating side relied on modifying MXene's hydrophilicity for adhesion, raising concerns about long-term reliability. Therefore, it is crucial to develop a high-performance thermal management

system that can switch between cooling and heating functions through physical flipping while ensuring long-term stability.

To achieve the above goals, two sources of infinite radiation cold and heat are employed: outer space (≈3 K) and the sun (≈5800 K),[14,35] which provide cooling and heating for buildings, respectively, without using other energy consumption. In this work, we developed a zero-energy dual-mode thermal management film that switches between heating and cooling functions through physical flipping of surface orientation, providing a solution for achieving high energy efficiency in building heating and cooling throughout the year. The two surfaces of the dual-mode film are divided into a cooling surface with radiative cooling and a heating surface with solar and Joule heating. This cooling function is realized through a porous structure exhibiting phase conversion using poly(vinylidene fluoride-co-hexafluoropropylene) [P-P(VDF-HFP)] and the hydrophobic SiO_2 (≈20 nm). This heating function is mainly achieved by graphene filter cake and carbon nanotube slurry, both of which have high solar absorption. Notably, the heating layer also has high electrical conductivity, it can achieve a saturation temperature of 96.7 ℃ by Joule heating under the voltage of 8 V. Consequently, the two heating modes' synergy each other lead to the achievement of the desired heating capacity, while dual-mode films can easily implement the surface conversion of cooling and heating by physical flipping.

RESULTS AND DISCUSSION

Structural View and Design Principle of Zero-Pollution Dual-Mode Films. Figure 1a shows the structural view of the dual-mode thermal management film and its preparing process is illustrated in Figure S1. The principle of dual-mode films in PRC and PSH modes are shown in Figure 1b and 1c, respectively. When the cooling

surface of the dual-mode thermal management film is in operation, it can effectively enhance the reflectance and scattering of sunlight due to its porous structure. Benefiting from SiO_2 particles attached to the cooling surface and P(VDF-HFP) are a kind of mid-infrared high-absorption material,[36] the high emission in the mid-infrared can be achieved by the cooling surface. Moreover, due to the extremely low surface energy of the P(VDF-HFP)[37,38] and the hydrophobic property of the SiO_2 particles, the whole cooling surface realizes functions of superhydrophobicity and self-cleaning. Instead, the heating surface realizes strong absorption of solar energy due to graphene and carbon nanotubes, resulting in zero-energy heating. Therefore, this dual-mode functional design enables the integration of cooling and heating in the thermal management film, making thermal regulation possible through physical flipping.

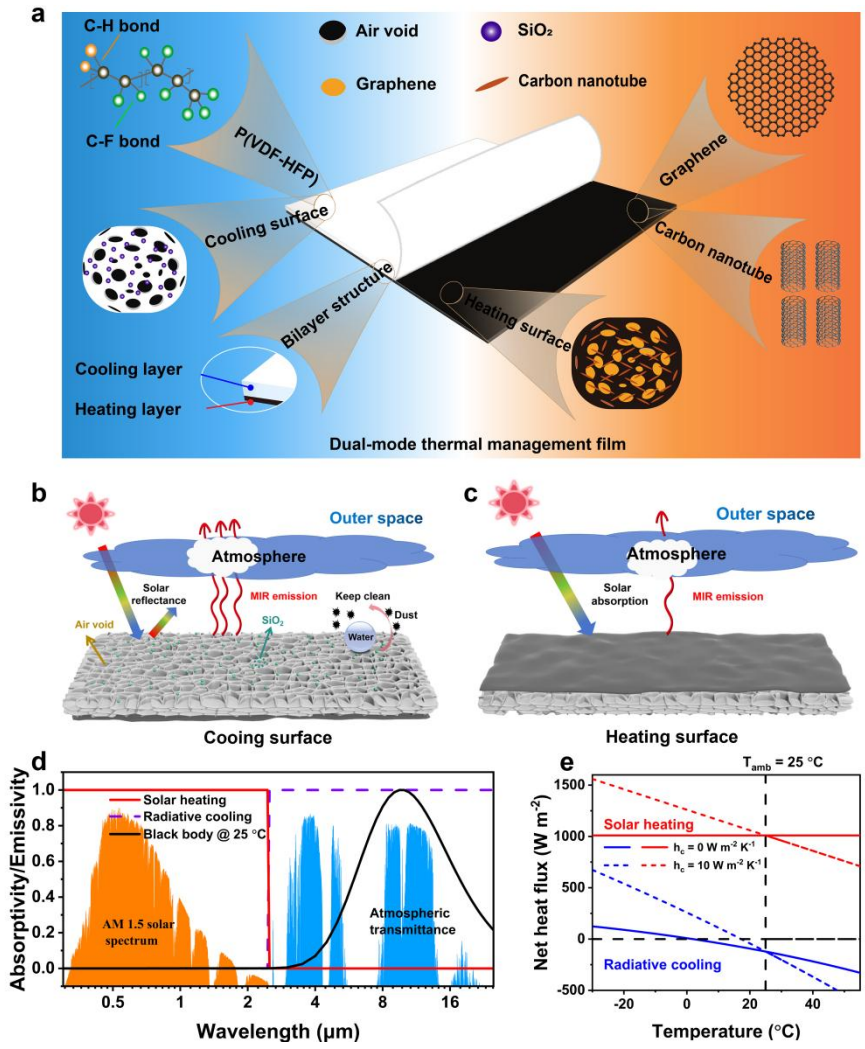

Figure 1. Overview of thermal management of dual-mode films for cooling and heating functions. (a) The porous P(VDF-HFP) with C-F and C-H bonds is combined with SiO_2 to obtain a superhydrophobic cooling surface with high reflectivity and high emissivity. The heating performance of the heating surface is determined by the graphene filter cake with 21 wt.% graphene, and carbon nanotube slurry with 15 wt.% nanotubes. (b) Working principle of the cooling surface. (c) Working principle of the heating surface. (d) Absorptivity/emissivity spectra of an ideal solar heating film (red line) and a radiative cooling (purple line) film. Transmittance spectrum of the atmosphere, $T_{atm}(\lambda)$ (blue), standard solar spectrum, $I_{AM1.5}(\lambda)$ (orange) and black body radiation spectrum at 25 ℃ (black). (e) Net heat flux at ideal solar heating (red) and radiative cooling (blue) temperatures.

To quantify the effects of PRC and PSH of dual-mode films, the net cooling power of the cooling surface and the net heating power of the heating surface were calculated. Here the net heat flux (P_{net}) is uniformly used to express net power, where negative P_{net} and positive P_{net} represent net cooling power and net heating power, respectively. The P_{net} is a function of the temperature of the dual-mode film (T_{film}) (Equation 1),[2,3] and it is determined by the heat balance among four key parts: the solar radiation absorbed from the sun (P_{sun}), the heat radiation absorbed from the atmosphere (P_{atm}), the heat emitted by the film (P_{film}), and the heat convection and conduction ($P_{cond+conv}$) of the dual-mode film with the surroundings, characterized by heat transfer coefficient (h) (Equation 2 and Note S1).[26]

$$P_{net} = P_{sun} + P_{atm} + P_{cond+conv} - P_{film} \quad (1)$$

$$P_{cond+conv} = h(T_{amb} - T_{film}) \quad (2)$$

Here, in Figure 1d, the absorptivity of the ideal cooling surface and heating

surface of the dual-mode film are fixed at 0 and 1 in the wavelength of 0.2-2.5 μm, respectively; the absorption of the ideal radiative cooling surface and heating surface are fixed at 1 and 0 within the 2.5-25 μm, respectively; the radiation spectrum of the blackbody at 25 ℃ is calculated. Meanwhile, the emissivity spectra of the blackbody from 0-50 ℃ were calculated (Figure S2), it demonstrates that the emissivity of around 10 μm is better for enhancing the radiative cooling effects of radiative coolers. In addition, the ambient temperature (T_{amb}) and P_{atm} were fixed at 25 °C and 310 W m^{-2}, respectively. When the P_{net} is zero, the film reaches the steady-state temperature, and thermal management power (negative for cooling and positive for heating) is the intersection point between T_{film} and T_{amb} (Figure 1e). Under cooling state (Figure 1e), the steady-state temperature of the film gradually approaches T_{amb} and the difference with T_{amb} decreases as the heat transfer coefficient increases (from 0 to 10 W m^{-2} K^{-1}), which is due to the fact that when T_{film} is lower than that of T_{amb}, the heat conduction and convection promote the film from the environment to energy acquisition. Unlike the steady-state temperature, the thermal management power is independent of h and it always remains at 121 W m^{-2}. This analysis also applies to the heating state. In heating state, the thermal management power can reach up to 1010 W m^{-2}. The analysis of the net heat flux function shows that our designed dual-mode film can effectively achieve cooling and heating capabilities.

Microstructures and Spectral Properties of Dual-Mode Films. The cooling surface appears white in sunlight and has a porous structure with pore size distribution of 0.4-8 μm and a 164° contact angle (Figure 2a, b), which makes the cooling surface has long-term stability of superhydrophobic (Note S2 and Figure S3) and self-cleaning properties (Figure S4). Moreover, the cooling surface will produce a silver mirror reaction and water sputtering (Figure S5), which is caused by the

trapping of air pockets inside the structure, so that the surface can remain dry underwater. The heating surface appears black in sunlight (Figure 2c), and the morphology and water contact angle of the heating surface are shown in Figure 2d. It is worth noting that the heating surface formed by the water-based polyurethane (WPU) allows all particles to be uniformly distributed and firmly fixed to the heating surface to avoid shedding, which improves the stability of the heating surface properties.

During the preparation process, the component concentration of the cooling surface is confirmed by analyzing the solar reflectivity and mid-infrared emissivity of porous films prepared with different P(VDF-HFP) contents in N,N-Dimethylformamide (DMF) solution. For example, in DMF solutions with a P(VDF-HFP) content of 15%, 20%, and 25%, the resulting porous samples are called P-P(VDF-HFP)-15, P-P(VDF-HFP)-20, and P-P(VDF-HFP)-25, respectively. A series of optical performance tests were performed on the above samples (Figure S6). The solar reflectivity of the above porous samples is 0.842, 0.895 and 0.855, respectively (Table S1). The difference in solar reflectivity is due to the different powder content, resulting in different pore sizes of porous films. The porosity results show that the higher the powder content, the lower the porosity of the obtained porous films (Figure S7). Porous films with lower powder content tend to have larger pores and higher light transmission, resulting in a reduction in solar reflectivity. However, their reflectivity still remains higher than that of the dense films (Figure S8). Moreover, porous films with higher powder content have smaller pores, denser films and lower scattering efficiency, which also reduces reflectivity. Similarly, the emissivities of the different films mentioned above in the mid-infrared were calculated according to Figure S6. The emissivity of all films is above 0.9 (Table S1), this is mainly due to the

P(VDF-HFP) material which has strong absorption in the mid-infrared (Figure S9).

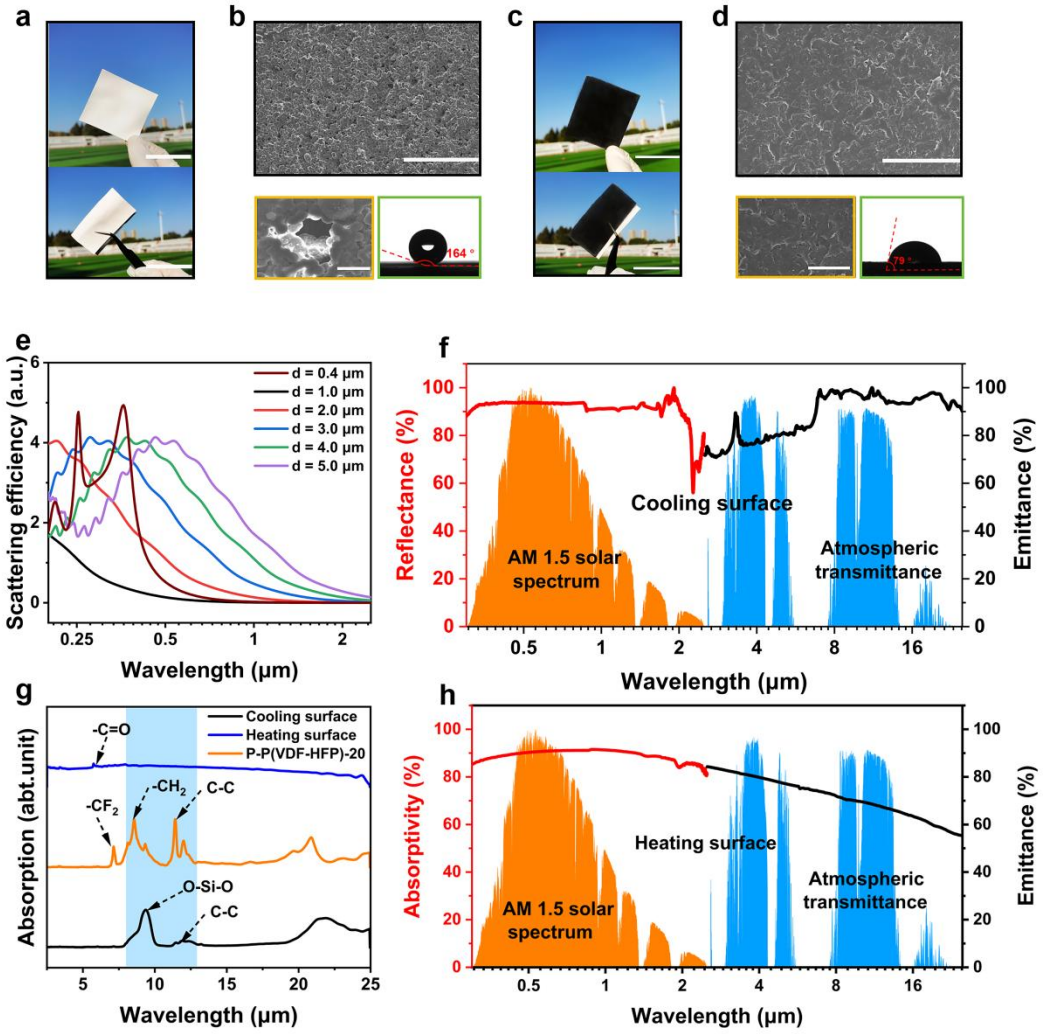

Figure 2. Microstructures and optical properties of cooling and heating surface of the dual-mode film. (a) Photos of the as-prepared cooling surface (scale bar = 2 cm). (b) The upper part is surface field-emission scanning electron microscopy (SEM) images of the cooling surface (scale bar = 300 μm), the bottom left part (scale bar = 5 μm) is enlarged view of the upper porous part and the bottom right part is the water contact angle of cooling surface. (c) Photos of the as-prepared heating surface (scale bar = 2 cm). (d) The upper part is SEM image of the heating surface (scale bar = 100 μm), the bottom left part (scale bar = 30 μm) is enlarged view of the upper part, while the bottom right part is the water contact angle of heating surface. (e) Simulated

scattering spectra of pores of different sizes. (f) Solar reflectivity in the solar region (0.3-2.5 μm) and thermal emissivity in the longwave infrared region (2.5-25 μm) of the cooling surface. (g) Fourier transform infrared spectroscopy (FTIR) spectra of the cooling surface, heating surface and P-P(VDF-HFP)-20. (h) Solar reflectivity in the solar region (0.3-2.5 μm) and thermal emissivity in the longwave infrared region (2.5-25 μm) of the heating surface.

Combined with the optical properties of the samples, the P-P(VDF-HFP)-20 was eventually chosen to be the part basis design of the cooling surface. The pore sizes of the cooling surface are obtained by SEM tests (Figure S10), and the sizes are widely distributed, mainly centered on 0.4-5 μm (Figure S11). Light undergoes multiple reflections at the pore wall-air interfaces, which effectively extends its travel path and enhances scattering. According to Mie scattering theory, strong scattering occurs when the pore size is comparable to the wavelength of light.[30] Larger pores increase the number of scattering interfaces, thereby amplifying the overall scattering effect. Moreover, the scattering efficiency is further improved by the size of the 0.4 μm nanopores, which strongly scatter short electromagnetic waves (Figure 2e). To further improve the comprehensive performance of the cooling surface, the hydrophobic SiO_2 particles were sprayed on the surface, and tested the mid-infrared reflectivity (Figure S12a) and mid-infrared transmissivity (Figure S12b) to obtain the mid-infrared emissivity (Figure 2f) of the cooling surface. The reflectivity of the cooling surface and P-P(VDF-HFP)-20 reaches 0.92 and 0.89, respectively. The reflectivity of the cooling surface is obviously better than that of P-P(VDF-HFP)-20, which is mainly caused by SiO_2. The nanoscale SiO_2 has excellent reflectance in the solar spectral region (Figure S13), thus improving the reflectance of the cooling surface.

The XPS patterns of cooling surface and P-P(VDF-HFP)-20 samples demonstrate

that the C, O, F are the main elementary components of both samples, and thermal resonant modes of chemical bonds such as C-F, C=O and C-H are observed in mid-infrared region[36] (Figure S14 and S15). Based on Kirchhoff's law, the emissivity of the cooler corresponds to its absorptivity, so these above porous films have excellent emissivity, with the emissivity of the cooling surface and P-P(VDF-HFP)-20 reaching 0.95, 0.94, respectively. Then, FTIR tests was performed on the cooling surface, heating surface, and P-P(VDF-HFP)-20 to analyze emissivity of samples (Figure 2g). The tiny difference of emissivity between cooling surface and P-P(VDF-HFP)-20 is due to SiO_2. The Si-O-Si chemical bond of the cooling surface located at the atmospheric transparent window (8-13 μm), which can improve the emissivity of the cooling surface. Therefore, the addition of SiO_2 can effectively improve both reflectivity and emissivity of the cooling surface.

Figure 2h shows the reflectivity and emissivity of the heating surface, it has high absorption (≈0.90, Table S2) in the sunlight region. It is mainly achieved by the graphene filter cake and carbon nanotube slurry, which have strong absorption in the sunlight region (Figure S16) and low absorption in mid-infrared region (Figure S17). Optical tests were performed on the three different heating surface samples fabricated in the experimental section of the article. The absorption of these heating surfaces containing different WPU ratio were tested in the solar band, with the increase of WPU content, the absorption of sunlight on the heating surface will be reduced (Figure S18). But benefiting from the stabilizing effect of WPU on the particles, the heating surface can maintain stable optical performance (Figure S19). After comparing the absorption and stabilization properties of these samples, the design of the heating surface in our dual-mode films was determined. Simultaneously, the effect of the WPU on the emissivity of the heating surface is tested (Figure S20), this result

shows that the emissivity of the heating surface containing the WPU is higher. To explain this result, XPS test was performed on the heating surface (Figure S21), the main elements of the heating surface are C, O, and N, with the N element coming from the WPU. A separate FTIR test was carried out on a pure WPU film (Figure S22), it shows that the WPU has a good absorption in the mid-infrared band, which will enhance the emissivity of the heating surface in the mid-infrared. Although WPU is not suitable for the ideal heating surface to obtain higher heating capacity, its stabilizing effect is necessary for dual-mode films. More importantly, according to Equation 1, when the film is at a high solar absorptive capacity and a moderate radiative capacity, it produces much more $P_{sun} + P_{atm}$ than the P_{film}, so that the effect of the WPU is minimal.

Indoor PRC, PSH and Joule Heating Performances of Dual-Mode Films. A test device consisting of foam box, polyethylene (PE) film (making samples and shielded air in the same experimental system), aluminum foil (minimizing the effects of heat convection and radiation from the surrounding environment), two dual-mode films (for heating and cooling surfaces respectively) and P-P(VDF-HFP)-20 was set up (Figure 3a). Meanwhile a xenon lamp (solar irradiance of 1000 W m^{-2}) was used to simulate the sunlight to co-verify the cooling and heating ability of dual-mode films. Since the emissivity of the heating surface is moderate, a thermal imaging camera can be used to monitor its actual temperature. The temperature of the three film samples remained consistent with the ambient temperature (≈19.1 °C) in the light-off condition (Figure 3b). When the light was turned on, the thermal image shows that the temperature of the cooling surface was lower than other samples, while the heating surface warmed up the fastest. Figure 3c shows that after turning on the light, all indoor temperatures rise sharply, and the rate of temperature rise gradually slows

down after some time and eventually reaches the saturation temperature. From the temperature difference curves (Figure 3d), it can be seen that after reaching the saturation temperature, the internal temperature of the cooling surface is 11.7 °C lower than the ambient temperature at most, and the cooling surface is 1.1 °C lower than that of the P-P(VDF-HFP)-20. Notably, the temperature of the heating surface is 18 °C higher than the ambient temperature. Indoor PSH mode of a house model (Figure S23) was tested, and its temperature has increased by 15.2 °C, which further proves that dual-mode films have great potential in the field of heating energy saving.

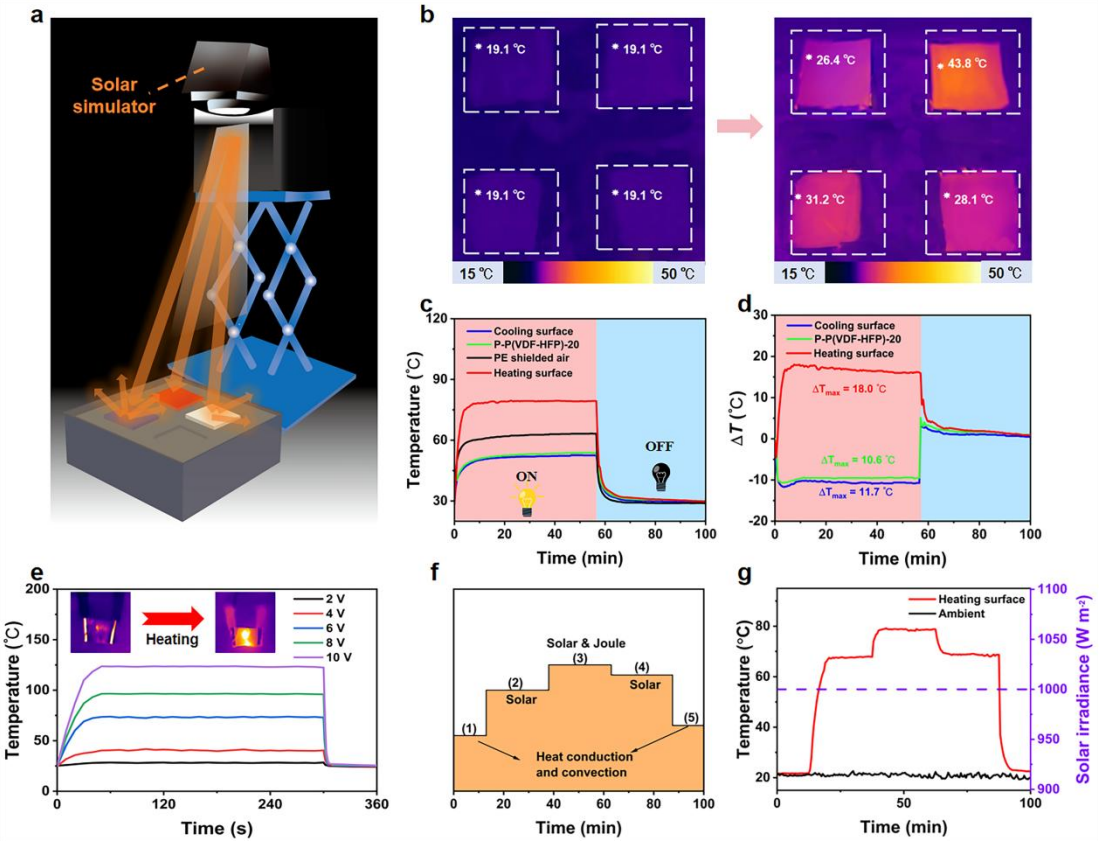

Figure 3. Indoor PRC, PSH and Joule heating tests. (a) Schematic diagram of indoor heating under xenon lamp irradiation. (b) Infrared images of cooling surface, heating surface and P-P(VDF-HFP)-20 before and after turning on the xenon lamp. (c) Real-time temperatures inside the three films and ambient air during testing. (d) Real-time temperature difference between the internal temperature of the three films

and the ambient temperature during testing. (e) Joule heating tests of dual-mode films at different voltages. (f) Steps for switching between PSH and Joule multimode heating regulation. (g) Real-time temperature curve of switching heating mode with indoor xenon lamp and power supply.

Graphene filter cakes and carbon nanotube slurry provide high electrical conductivity to dual-mode films and can be employed as active heaters for unexpected situations. With the increase of the applied DC voltage time, the maximum temperature of dual-mode films is 28.1 °C, 40.2 °C, 73.3 °C, 96.2 °C and 123.3 °C at 2, 4, 6, 8 and 10 V, respectively (Figure 3e). Simultaneously, at the same voltage, with the increase of heating time, the heated region of the thermal infrared image becomes more significant and uniform (Figure S24). It has been shown that dual-mode films have fast electrothermal response and high efficiency of electrothermal conversion, providing applications for joint work of PSH and Joule heating. In order to explore the heating capacity of PSH and Joule heating in alternating and co-operating modes of operation, the work is studied in accordance with the program steps (Figure 3f). Figure 3g shows that the dual-mode film is in an indoor environment (21.6 °C) in the first stage and enters the second stage after a period of time. The dual-mode film was in PSH single heating mode in the second stage, and when it has reached its saturation temperature (67.7 °C). A voltage of 3 V was passed on the film, so that its heating mode was in the combined mode of PSH and Joule heating (third stage). Then the heating saturation temperature raised from 67.7 °C to 78.9 °C, and then the power was cut off to make it re-enter the PSH heating mode (fourth stage), and its temperature gradually maintained at 68.8 °C, which suggests that the dual-mode film continues to exhibit excellent PSH heating. Eventually, the xenon lamp was turned off (fifth stage), and the temperature of the dual-mode film gradually approached room temperature

and its corresponding infrared images were shown in Figure S25. Therefore, these experimental results clearly demonstrate that PSH and Joule heating can be used together for all-weather multimode heating.

Outdoor PRC and PSH Performances of Dual-Mode Films. Figure 4a shows the prepared large size dual-mode film. In Figure 4b, the experimental setup was built in *Hangzhou* to evaluate the outdoor cooling and heating capabilities of dual-mode films and the actual outdoor device is shown in Figure S26. On October 21, 2023, the weather was sunny with a level 1 breeze, the effects of PRC and PSH for dual-mode films were performed. Under direct sunlight with the solar irradiance of 853.88 W m^{-2}, the cooling temperatures of the cooling surface and P-P(VDF-HFP)-20 were 13.3 °C and 6.7 °C lower than the ambient temperature, respectively, and the temperature of the heating surface was 11.4 °C higher than the ambient temperature (Figure 4c, d). To illustrate that the dual-mode films are capable of a wide range of weather conditions, outdoor test was also conducted on cloudy weather (October 24, 2023), it achieved an average warming of 7.3 °C and a cooling capacity of 3.7 °C (Note S3 and Figure S27). The weather was overcast with a breeze index of level 2 and a relative humidity of 52-86% on October 25, 2023 and the average solar irradiance was only 606 W m^{-2} from 11 am to 2 pm (Figure 4e). But the cooling surface temperature can also achieve 6.5 °C lower than the ambient temperature and compared with the P-P(VDF-HFP)-20. Moreover, the cooling surface was 2.1 °C cooler than the P-P(VDF-HFP)-20, and the heating surface can achieve a temperature rise of 6.2 °C (Figure 4f). These results indicate that dual-mode films have excellent cooling and heating capacities, and the outdoor air humidity and temperature information above are provided in Figure S28. Furthermore, we conducted weatherability tests on the dual-mode films, and the spectral changes were minimal, demonstrating their

long-term durability (Figure S29).

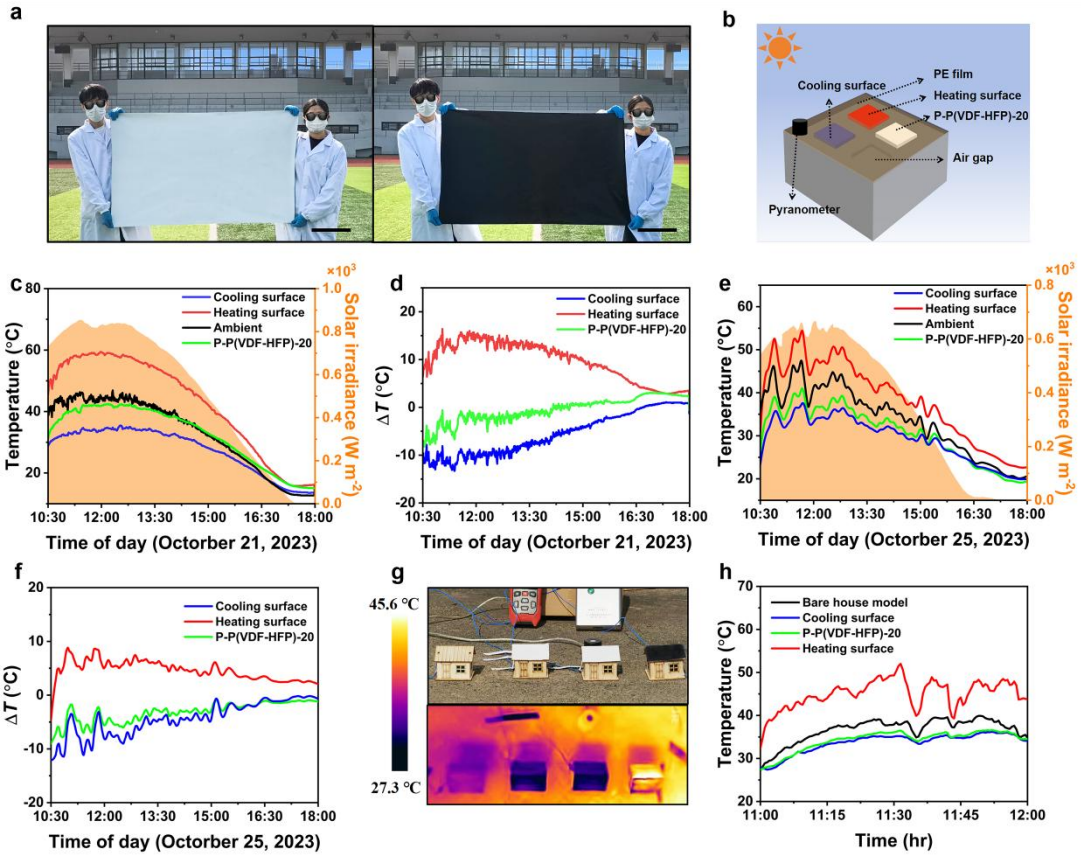

Figure 4. Outdoor PRC and PSH performances of dual-mode films. (a) Photograph of the dual-mode film (scale bar = 20 cm). The left part is the photograph of cooling surface and the right part is the photograph of heating surface. (b) Model drawing of the experimental device. (c) Real-time temperature records of all film samples on October 21, 2023. (d) The temperature difference among all film samples and the ambient environment at daytime (October 21, 2023). (e) Real-time temperature records of all film samples on October 25, 2023. (f) The temperature difference among all film samples and the ambient environment at daytime (October 25, 2023). (g) The digital photographs and thermal infrared images of the house models. (h) Real-time temperature records of house models on November 23, 2023.

In order to better illustrate the promising application of dual-mode films for

practical outdoor cooling and heating modes. The cooling and heating surfaces of dual-mode films and P-P(VDF-HFP)-20 were used to cover the surface of the car models (the car model achieves an average of 12.7 °C subambient cooling, Figure S30) and house models (Figure 4g). From 11:00 am to 12:00 am, compared with the bare house model, the interior of the house under the heating surface and the cooling surface achieved an average temperature rise of 8.4 °C and a temperature drop of 3.1 °C (Figure 4h and Figure S31), respectively. In addition, a flame retardant test was conducted on the dual-mode film (Note S4 and Figure S32). Due to the excellent thermal conductivity of the graphene filter cakes and carbon nanotube slurry, the excess heat in the localized region can be quickly transferred to the rest of the film, so that the heat is well dispersed and no solution dripping is formed. Ideal mechanical properties are also the reference metrics for outdoor films, so stress-strain and cyclic tensile tests were performed on different film samples. The dual-mode film has excellent mechanical properties, being able to withstand a tension of 10.5 N, elongation by 53%, and still maintaining good mechanical properties under multiple periodic stretches (Figure S33).

Potential Applications of Dual-Mode Films in Building Energy Saving and Carbon Emission Reduction. To evaluate the potential sustainability of dual-mode films, an energy estimation model has been developed to quantify the energy savings and carbon emission reductions that can be achieved by integrating dual-mode films onto the roof of a building. Figure 5a illustrates the global distribution of solar irradiance.[39] Some extremely hot and cold regions urgently require cooling and heating to alleviate environmental discomfort. The EnergyPlus software was utilized to simulate the energy consumption of a building using dual-mode films in terms of heating, ventilation, and air conditioning (HVAC). Based on the building model

defined by the US Department of Energy,[40,41] a Medium Office building was selected to estimate the annual energy usage per unit area (Note S5, Figures S34-36, and Tables S3 and S4). The globe is divided into 30 climate zones by the Köppen climate classification.[42] The total annual energy savings from installing dual-mode films on the roofs of seven typical cities in different climate zones were simulate (Table S5). As shown in Figure 5b, in the place where there is an obvious temperature difference in a year (Turpan), the total energy can be saved by 51.64 MJ m^{-2} per year. In Singapore, the temperature is high all year round, the application of the cooling mode of the dual-mode films can achieve up to 123.07 MJ m^{-2} cooling energy saving. Even in areas with low solar irradiance (Oslo), 7.19 MJ m^{-2} heating savings can be achieved.

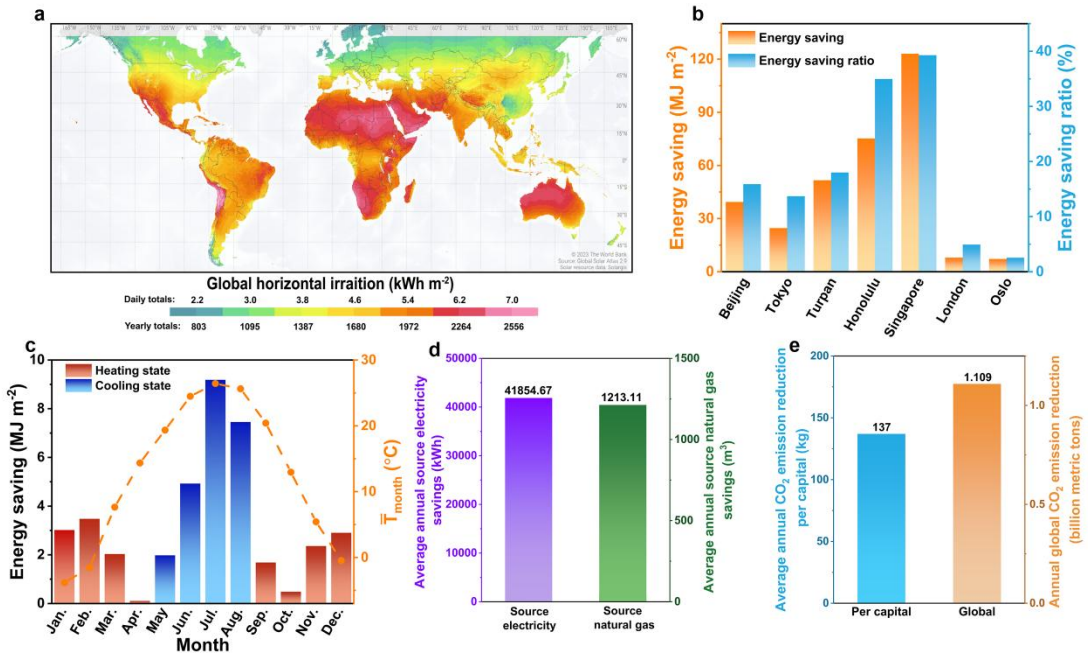

Figure 5. Estimated energy savings and carbon emission reductions. (a) Global solar irradiation flux, adapted with permission under a Creative Commons Attribution-ShareAlike 4.0 (CC BY-SA 4.0) license from ©2021 Solargis. Source: Global Solar Atlas 2.0, Solar resource data; Solargis. Copyright ©2021 Solargis.[39] (b)

Average annual energy savings per unit area of buildings in different cities. (c) Energy savings in Beijing in different months. (d) Estimate the average annual energy savings of source electricity and source natural gas for a Medium Office building (e) Predicted per capita and global average annual CO_2 reductions.

To better demonstrate the energy-saving applications of our dual-mode films, Beijing was selected for specific energy-saving analysis. As shown in Figure 5c, with reference to the historical meteorological data and according to the average temperature of each month in Beijing, different working modes were chosen for the roof films of the building. In May, June, July and August, the cooling mode is selected and the heating mode is selected for the remaining months. In the cold winter (e.g., January), the total solar radiation is very low, but due to the high solar absorption of dual-mode films, considerable heat is still achieved (energy saving ≈3.02 MJ m^{-2}). In the hot summer (e.g., July), excellent cooling capacity is also achieved (energy saving ≈9.19 MJ m^{-2}). It is worth noting that buildings utilizing dual-mode films save up to 15.89% energy per year in Beijing. Furthermore, the building's annual energy savings in Beijing were converted into annual savings of source electricity and source natural gas savings (Figure 5d). According to the calculations using EnergyPlus, the building saves an average of 41 854.67 kWh of source electricity and 1 213.11 m^3 of source natural gas per year, which equates to a reduction of 36 668 kg of CO_2 emissions for the entire building and 137 kg of CO_2 emissions per capita. Based on the world's population, our estimate of CO_2 emission reductions is 1.109 billion metric tons (Figure 5e), which is equivalent to about 3% of current global CO_2 emissions (i.e., 36.4 billion metric tons per year[43,44]). The above results show that dual-mode films have excellent year-round energy-saving performance, reproducibility, and scalability, making them suitable for large-scale applications not only in buildings but also in

transportation, where thermal management is required (Figure S37).

CONCLUSION

In summary, we reported a zero-energy and zero-pollution dual-mode thermal management film designed by using natural renewable resources (solar heating and space cooling), which can be used for all-weather radiative cooling and solar heating. In practical applications, under direct sunlight with the solar irradiance of 853.88 W m^{-2}, the dual-mode film achieved a temperature rise of 11.4 °C and a temperature drop of 13.3 °C. Moreover, we compared our work with the previous works, and successfully summarized three typical characteristics of dual-mode films (Figure S38, Table S6): (a) dual-mode films have excellent optical properties in both heating and cooling modes to obtain dual-mode high thermal management performances. (b) Multiple ways of heating, passive solar absorption and Joule heating, which can cope with a variety of complex weather conditions. (c) The high efficiency of dual-mode films in outdoor cooling and heating demonstrate their potential for energy saving and carbon emission reduction in buildings. The combination of these three characteristics contributes to the stable and efficient cooling and heating capabilities of dual-mode films. Notably, the simulation results demonstrate that the dual-mode film can successfully achieve the effect of year-round energy saving by using the dual-mode working mode on the building roof, especially in the areas with obvious climate differences (e.g., Beijing). A series of results generated by energy saving, such as electricity and natural gas saving, can reduce CO_2 emissions, which is conducive to achieving the goal of carbon neutrality by 2050 and a better response to global climate change.

EXPERIMENTAL SECTION

Materials. Poly(vinylidene fluoride-co-hexafluoropropylene) [P(VDF-HFP)] powder was purchased from Arkema Investment Co., Ltd.. The dimethylformamide (DMF, 99.5%) and hydrophobic silica (SiO_2, ≈20 nm) were bought from Shanghai Macklin Biochemical Co., Ltd.. Water-based graphene filter cake with 21 wt.% graphene, water-based carbon nanotube slurry with 15 wt.% nanotubes, and water-based polyurethane were purchased from Suqian Tene Valley Nano Technology Co., Ltd., China.

Preparation of Heating Solutions. After the optimal graphene filter cake to carbon nanotube slurry ratio of 1:1 was determined (Figure S39), the effect of WPU on the heating surface was investigated. The water-based graphene filter cake, water-based carbon nanotube slurry, water-based polyurethane (WPU) and deionized water were prepared into mixed solutions according to 2:2:0.5:2, 2:2:1:2 and 2:2:1.5:2 respectively. These heating surface made with different weight percentages of the above WPU were donated as heating surface-1, heating surface-2, heating surface-3, respectively. These solutions were then placed on a mixing table and stirred for one hour at room temperature at 600 rpm to obtain a homogeneous mixture of heating solution.

Preparation of Dual-Mode Films. P(VDF-HFP) powder and DMF were added into a beaker and stirred at 35 °C for one hour to form a P(VDF-HFP) casting solutions with solute weight percentages of 15%, 20% and 25%, respectively. Subsequently, different weight percentages of P(VDF-HFP) casting solutions were poured onto glass plates, evenly scraped with a glass rod, and then placed in an oven at 30 ℃ for 30 minutes to obtain the pure P(VDF-HFP) films that were not completely dried. Immediately afterward, the pure films were placed in deionized water for 10 hours to obtain the semi-transparent P(VDF-HFP) films, and then the

films were placed in an oven at 25 ℃ to dry for 24 hours, and finally we can obtain different weight percentages of porous P(VDF-HFP) films [P-P(VDF-HFP)]. The above P-P(VDF-HFP) samples with different weight percentages were named P-P(VDF-HFP)-15, P-P(VDF-HFP)-20, P-P(VDF-HFP)-25, respectively. Based on the influence of SiO_2 on the reflectance of the cooling surface (Figure S40), the optimal ratio of DMF to SiO_2 was determined to be 1:0.2, and the solution was sprayed on the surface of P-P(VDF-HFP) samples using a spray gun, then dried in an oven at 50 ℃ for one hour to get the cooling surface of the dual-mode film. In a similar way, the heating solution was sprayed on the other surface of P-P(VDF-HFP) samples using a spray gun and was left at room temperature for 20 minutes to obtain the heating surface of the dual-mode film. If not otherwise specified, the thickness of all dual-mode films used in the experiments was 680 μm, with a cooling surface of 610 μm and a heating surface of 70 μm. The design of the cooling surface thickness was optimized to achieve the best cooling performance, as shown in Figure S41.

Optical Characterization. An UV/VIS/NIR spectrophotometer (Shimadzu UV-3600) was employed to test the reflectivity of the samples in the solar radiation band (0.3-2.5 μm). The Nicolet iS50 was used to measure the emittance of samples in the mid-infrared (2.5-25 μm). The morphologies of P-P(VDF-HFP) samples and dual-mode films were characterized using surface field-emission scanning electron microscopy (SEM, Hitachi Regulus8100), and the elements of cooling surface was measured by energy dispersive spectroscopy (EDS) module. The chemical composition of all film samples was observed using an X-ray photoelectron spectrometer (XPS, Thermo Scientific K-Alpha). Fourier transform infrared spectroscopy (FTIR, Thermo Nicolet iS5) was employed to measure absorption of cooling surface, heating surface and pure WPU film in mid-infrared. The static water

contact angle of the cooling surface of dual-mode film and P-P(VDF-HFP) were measured using an optical contact angle measuring device (Dataphysics DCAT21). A G-DenPyc 2900 true density tester was utilized to examine the true density of porous films, and an infrared camera (FLIR ONE PRO) was used to capture the instantaneous temperature of film samples.

Practical Evaluations. In order to better show the tensile strength of films, we made rectangular film samples (2 × 2 cm^2 in size) for tensile strength testing. The mechanical tensile test of films were performed using the SH-100N explicit push-pull force meter with a DC motor. The combustion tests were performed on an alcohol burner where the sample (3 × 3 cm^2 in size) was ignited by the flame. The burning process was recorded by a smartphone.

Indoor Cooling/Heating Performance Measurement. Polystyrene foam was used to prepare the cooling/heating performance design due to its ability to minimize the effects of ambient heat conduction. Four cavities (4 × 4 × 4 cm^3) were dug out of the polystyrene foam (30 × 30 × 20 cm^3), and then the foam was wrapped in aluminum foil to reduce the foam's absorption of sunlight, in which the four cavities were exposed to the outside. Then these sample films (5 × 5 cm^2) were placed on these cavities, the K-type thermocouples were fixed in the cavities, and the edges of samples were sealed with tape to ensure the accuracy of the test data in cavities. And the top of the foam box was sealed with polyethylene (PE) film to keep the temperature of all the samples and the shielding air in the same experimental system. Then the foam unit and the house model (58 × 47 × 49 mm^3) were used for the indoor PRC and PSH tests, and the indoor simulation tests were performed under a solar radiation of 1000 W m^{-2} with the xenon lamp. Joule heating test was tested using a DC power supply. We connected both ends of the dual-mode film (3 × 2 cm^2) to the

positive and negative terminals of the power supply device, and output different voltages through the DC power to obtain the heating capacity of the film at different voltages. The Joule heating and PSH cooperative performance were evaluated by applying DC voltage to both ends of a dual-mode film (6 × 3 cm^2) and sunlight exposure under a xenon lamp, and the surface temperature was recorded by infrared thermal camera.

Outdoor Cooling/Heating Performance Measurement. The same foam units used for the indoor tests were used for the outdoor PRC and PSH tests. At the same time, a solar radiometer was used to record the real-time solar irradiance. In addition, the houses (58 × 47 × 49 mm^3) and cars (75 × 30 × 25 mm^3) simulators were used to test the dual-mode film's cooling and heating properties. Samples were cut to size for each model and then covered the tops of houses and the roofs of cars. Similarly, K-type thermocouples were employed to test the temperature inside houses and cars, and the infrared thermal camera was employed to record their infrared images. All the outdoor tests were conducted at China Jiliang University.

ASSOCIATED CONTENT

Supporting Information. Properties of dual-mode films, spectral reflectivity/emissivity of the cooling surface with different thickness, net cooling power calculation, FTIR spectra of WPU and dual-mode film, schematic and photograph of outdoor measurement setup, temperature and relative humidity during outdoor measurement, cooling performance of the dual-mode film outdoors.

AUTHOR INFORMATION

Corresponding Author

Gongxun Bai - *College of Optical and Electronic Technology, China Jiliang University, Hangzhou 310018, P. R. China;* Email: baigx@cjlu.edu.cn

Peng Xue - *Beijing Key Laboratory of Green Building Environment and Energy Saving Technology, Beijing University of Technology, Beijing 100124, P. R. China;* Email: xp@bjut.edu.cn

Jianhua Hao - *Department of Applied Physics, The Hong Kong Polytechnic University, Hong Kong 999077, P. R. China;* Email: jh.hao@polyu.edu.hk

Authors

Ruiming Tan - *College of Optical and Electronic Technology, China Jiliang University, Hangzhou 310018, P. R. China*

Cuilu Xi - *College of Optical and Electronic Technology, China Jiliang University, Hangzhou 310018, P. R. China*

Yuxin Ma - *Beijing Key Laboratory of Green Building Environment and Energy Saving Technology, Beijing University of Technology, Beijing 100124, P. R. China*

Yinyan Li - *College of Optical and Electronic Technology, China Jiliang University, Hangzhou 310018, P. R. China*

Beibei Xu - *State Key Laboratory of Modern Optical Instrumentation, School of Optical Science and Engineering, Zhejiang University, Hangzhou 310027, P. R. China*

Shiqing Xu - *College of Optical and Electronic Technology, China Jiliang University, Hangzhou 310018, P. R. China*

Author Contributions

R.M.T. conceived the idea and made further innovations. J.H.H., G.X.B., S.Q.X and B.B.X. supervised the work and guided the project. R.M.T. and C.L.X. fabricated the dual-mode films, conducted the microstructures and spectral characterizations, and analyzed the application of dual-mode films under G.X.B.'s supervision. P.X. and Y.X.M. use the EnergyPlus software to build an energy model for energy saving calculation. R.M.T., G.X.B. and Y.Q.L. analyzed the data. All the authors discussed the results and commented on the manuscript.

Notes

The authors declare no competing financial interest.

ACKNOWLEDGMENTS

Financial support of the National Key Research and Development Project of China (2021YFB3502100), and Zhejiang Provincial Natural Science Foundation of China (LR24F050002) are gratefully acknowledged.

REFERENCES

(1) Zeng, S.; Pian, S.; Su, M.; Wang, Z.; Wu, M.; Liu, X.; Chen, M.; Xiang, Y.; Wu, J.; Zhang, M.; Cen, Q.; Tang, Y.; Zhou, X.; Huang, Z.; Wang, R.; Tunuhe, A.; Sun, X.; Xia, Z.; Tian, M.; Chen, M.; Ma, X.; Yang, L.; Zhou, J.; Zhou, H.; Yang, Q.; Li, X.; Ma, Y.; Tao, G. Hierarchical-Morphology Metafabric for Scalable Passive Daytime Radiative Cooling. *Science* **2021**, *373*, 692-696.

(2) Xue, X.; Qiu, M.; Li, Y.; Zhang, Q. M.; Li, S.; Yang, Z.; Feng, C.; Zhang, W.; Dai, J.; Lei, D.; Jin, W.; Xu, L.; Zhang, T.; Qin, J.; Wang, H.; Fan, S. Creating an

Eco-Friendly Building Coating with Smart Subambient Radiative Cooling. *Adv. Mater.* **2020**, *32*, 1906751.

(3) Zhang, Q.; Lv, Y.; Wang, Y.; Yu, S.; Li, C.; Ma, R.; Chen, Y. Temperature-Dependent Dual-Mode Thermal Management Device with Net Zero Energy for Year-Round Energy Saving. *Nat. Commun.* **2022**, *13*, 4874

(4) Fan, C.; Long, Z.; Zhang, Y.; Mensah, A.; He, H.; Wei, Q.; Lv, P. Robust Integration of Energy Harvesting with Daytime Radiative Cooling Enables Wearing Thermal Comfort Self-Powered Electronic Devices. *Nano Energy* **2023**, *116*, 108842.

(5) Xu, J.; Huo, X.; Yan, T.; Wang, P.; Bai, Z.; Chao, J.; Yang, R.; Wang, R.; Li, T. All-in-One Hybrid Atmospheric Water Harvesting for All-Day Water Production by Natural Sunlight and Radiative Cooling. *Energy Environ. Sci.* **2024**, *17*, 4988–5001.

(6) Camarasa, C.; Mata, É.; Navarro, J. P. J.; Reyna, J.; Bezerra, P.; Angelkorte, G. B.; Feng, W.; Filippidou, F.; Forthuber, S.; Harris, C.; Sandberg, N. H.; Ignatiadou, S.; Kranzl, L.; Langevin, J.; Liu, X.; Müller, A.; Soria, R.; Villamar, D.; Dias, G. P.; Wanemark, J.; Yaramenka, K. A Global Comparison of Building Decarbonization Scenarios by 2050 towards 1.5–2 °C Targets. *Nat. Commun.* **2022**, *13*, 3077.

(7) Gillingham, K. T.; Huang, P.; Buehler, C.; Peccia, J.; Gentner, D. R. The Climate and Health Benefits from Intensive Building Energy Efficiency Improvements. *Sci. Adv.* **2021**, *7*, eabg0947.

(8) Shi, S.; Lv, P.; Valenzuela, C.; Li, B.; Liu, Y.; Wang, L.; Feng, W. Scalable Bacterial Cellulose-Based Radiative Cooling Materials with Switchable Transparency for Thermal Management and Enhanced Solar Energy Harvesting. *Small* **2023**, *19*, 2301957.

(9) Chen, Y.; Mandal, J.; Li, W.; Smith-Washington, A.; Tsai, C.-C.; Huang, W.; Shrestha, S.; Yu, N.; Han, R. P. S.; Cao, A.; Yang, Y. Colored and Paintable Bilayer Coatings with High Solar-Infrared Reflectance for Efficient Cooling. *Sci. Adv.* **2020**, *6*, eaaz5413.

(10) Goldstein, E. A.; Raman, A. P.; Fan, S. Sub-Ambient Non-Evaporative Fluid Cooling with the Sky. *Nat. Energy* **2017**, *2*, 17143.

(11) Xie, W.; Xiao, C.; Sun, Y.; Fan, Y.; Zhao, B.; Zhang, D.; Fan, T.; Zhou, H. Flexible Photonic Radiative Cooling Films: Fundamentals, Fabrication and Applications. *Adv. Funct. Mater.* **2023**, *33*, 2305734.

(12) Zhou, K.; Li, W.; Patel, B. B.; Tao, R.; Chang, Y.; Fan, S.; Diao, Y.; Cai, L. Three-Dimensional Printable Nanoporous Polymer Matrix Composites for Daytime Radiative Cooling. *Nano Lett.* **2021**, *21*, 1493–1499.

(13) Xiong, L.; Wei, Y.; Chen, C.; Chen, X.; Fu, Q.; Deng, H. Thin Lamellar Films with Enhanced Mechanical Properties for Durable Radiative Cooling. *Nat. Commun.* **2023**, *14*, 6129.

(14) Zhao, X.; Li, T.; Xie, H.; Liu, H.; Wang, L.; Qu, Y.; Li, S. C.; Liu, S.; Brozena, A. H.; Yu, Z.; Srebric, J.; Hu, L. A Solution-Processed Radiative Cooling Glass. *Science* **2023**, *382*, 684–691.

(15) Lin, K.; Chen, S.; Zeng, Y.; Ho, T. C.; Zhu, Y.; Wang, X.; Liu, F.; Huang, B.; Chao, C. Y.-H.; Wang, Z.; Tso, C. Y. Hierarchically Structured Passive Radiative Cooling Ceramic with High Solar Reflectivity. *Science* **2023**, *382*, 691–697.

(16) Bhatia, B.; Leroy, A.; Shen, Y.; Zhao, L.; Gianello, M.; Li, D.; Gu, T.; Hu, J.; Soljačić, M.; Wang, E. N. Passive Directional Sub-Ambient Daytime Radiative Cooling. *Nat. Commun.* **2018**, *9*, 5001.

(17) Guo, N.; Yang, R.; Chen, M.; Yan, H.; Chen, W. Self-Adaptive Colored Radiative Cooling by Tuning Visible Spectra. *Solar RRL* **2023**, *7*, 2300512.

(18) Zhao, D.; Aili, A.; Zhai, Y.; Xu, S.; Tan, G.; Yin, X.; Yang, R. Radiative Sky Cooling: Fundamental Principles, Materials, and Applications. *Appl. Phys. Rev.* **2019**, *6*, 021306.

(19) Yang, M.; Zhong, H.; Li, T.; Wu, B.; Wang, Z.; Sun, D. Phase Change Material Enhanced Radiative Cooler for Temperature-Adaptive Thermal Regulation. *ACS Nano* **2023**, *17*, 1693–1700.

(20) Li, X.; Xu, H.; Yang, Y.; Li, F.; Ramakrishna, S.; Yu, J.; Ji, D.; Qin, X. Selective Spectral Absorption of Nanofibers for Color-Preserving Daytime Radiative Cooling. *Mater. Horiz.* **2023**, *10*, 2487–2495.

(21) Wu, X.; Wang, Y.; Liang, X.; Zhang, Y.; Bi, P.; Zhang, M.; Li, S.; Liang, H.; Wang, S.; Wang, H.; Lu, H.; Zhang, Y. Durable Radiative Cooling Multilayer Silk Textile with Excellent Comprehensive Performance. *Adv. Funct. Mater.* **2023**, *34*, 2313539.

(22) So, S.; Yun, J.; Ko, B.; Lee, D.; Kim, M.; Noh, J.; Park, C.; Park, J.; Rho, J. Radiative Cooling for Energy Sustainability: From Fundamentals to Fabrication Methods Toward Commercialization. *Adv. Sci.* **2023**, *11*, 2305067.

(23) Gamage, S.; Kang, E. S. H.; Åkerlind, C.; Sardar, S.; Edberg, J.; Kariis, H.; Ederth, T.; Berggren, M.; Jonsson, M. P. Transparent Nanocellulose Metamaterial

Enables Controlled Optical Diffusion and Radiative Cooling. *J. Mater. Chem. C* **2020**, *8*, 11687–11694.

(24) Guo, C.; Tang, H.; Wang, P.; Xu, Q.; Pan, H.; Zhao, X.; Fan, F.; Li, T.; Zhao, D. Radiative Cooling Assisted Self-Sustaining and Highly Efficient Moisture Energy Harvesting. *Nat. Commun.* **2024**, *15*, 6100.

(25) Zhang, Y.; Chen, Y.; Wang, T.; Zhu, Q.; Gu, M. Ultrahigh Performance Passive Radiative Cooling by Hybrid Polar Dielectric Metasurface Thermal Emitters. *Opto-Electron. Adv.* **2024**, *7*, 230194.

(26) Wang, S.; Wu, Y.; Pu, M.; Xu, M.; Zhang, R.; Yu, T.; Li, X.; Ma, X.; Su, Y.; Tai, H.; Guo, Y.; Luo, X. A Versatile Strategy for Concurrent Passive Daytime Radiative Cooling and Sustainable Energy Harvesting. *Small* **2023**, 2305706.

(27) Cai, W.; Lin, B.; Qi, L.; Cui, T.; Li, Z.; Wang, J.; Li, S.; Cao, C.; Rahman, M. Z.; Hu, X.; Yu, R.; Shi, S.; Xing, W.; Hu, Y.; Zhu, J.; Fei, B. Bio-Based and Fireproof Radiative Cooling Aerogel Film: Achieving Higher Sustainability and Safety. *Chem. Eng. J.* **2024**, *488*, 150784.

(28) Abraham, E.; Cherpak, V.; Senyuk, B.; Ten Hove, J. B.; Lee, T.; Liu, Q.; Smalyukh, I. I. Highly Transparent Silanized Cellulose Aerogels for Boosting Energy Efficiency of Glazing in Buildings. *Nat. Energy* **2023**, *8*, 381–396.

(29) Ma, J.-W.; Zeng, F.-R.; Lin, X.-C.; Wang, Y.-Q.; Ma, Y.-H.; Jia, X.-X.; Zhang, J.-C.; Liu, B.-W.; Wang, Y.-Z.; Zhao, H.-B. A Photoluminescent Hydrogen-Bonded Biomass Aerogel for Sustainable Radiative Cooling. *Science* **2024,** *385*, 68–74.

(30) Wang, Y.; Wang, T.; Liang, J.; Wu, J.; Yang, M.; Pan, Y.; Hou, C.; Liu, C.; Shen, C.; Tao, G.; Liu, X. Controllable-Morphology Polymer Blend Photonic Metafoam for Radiative Cooling. *Mater. Horiz.* **2023**, *10*, 5060–5070.

(31) Qi, G.; Tan, X.; Tu, Y.; Yang, X.; Qiao, Y.; Wang, Y.; Geng, J.; Yao, S.; Chen, X. Ordered-Porous-Array Polymethyl Methacrylate Films for Radiative Cooling. *ACS Appl. Mater. Interfaces* **2022**, *14*, 31277–31284.

(32) Wang, H.-D.; Xue, C.-H.; Ji, Z.-Y.; Huang, M.-C.; Jiang, Z.-H.; Liu, B.-Y.; Deng, F.-Q.; An, Q.-F.; Guo, X.-J. Superhydrophobic Porous Coating of Polymer Composite for Scalable and Durable Daytime Radiative Cooling. *ACS Appl. Mater. Interfaces* **2022**, *14*, 51307–51317.

(33) Li, X.; Sun, B.; Sui, C.; Nandi, A.; Fang, H.; Peng, Y.; Tan, G.; Hsu, P.-C. Integration of Daytime Radiative Cooling and Solar Heating for Year-Round Energy Saving in Buildings. *Nat. Commun.* **2020**, *11*, 6101.

(34) Shi, M.; Song, Z.; Ni, J.; Du, X.; Cao, Y.; Yang, Y.; Wang, W.; Wang, J. Dual-Mode Porous Polymeric Films with Coral-like Hierarchical Structure for All-Day Radiative Cooling and Heating. ACS Nano 2023, 17, 2029–2038.

(35) Tang, K.; Dong, K.; Li, J.; Gordon, M. P.; Reichertz, F. G.; Kim, H.; Rho, Y.; Wang, Q.; Lin, C.-Y.; Grigoropoulos, C. P.; Javey, A.; Urban, J. J.; Yao, J.; Levinson, R.; Wu, J. Temperature-Adaptive Radiative Coating for All-Season Household Thermal Regulation. *Science* **2021**, *374*, 1504–1509.

(36) Qin, M.; Han, H.; Xiong, F.; Shen, Z.; Jin, Y.; Han, S.; Usman, A.; Zhou, J.; Zou, R. Vapor Exchange Induced Particles-Based Sponge for Scalable and Efficient Daytime Radiative Cooling. *Adv. Funct. Mater.* **2023**, *33*, 2304073.

(37) Tian, Y.; Shao, H.; Liu, X.; Chen, F.; Li, Y.; Tang, C.; Zheng, Y. Superhydrophobic and Recyclable Cellulose-Fiber-Based Composites for High-Efficiency Passive Radiative Cooling. *ACS Appl. Mater. Interfaces* **2021**, *13*, 22521–22530.

(38) Hu, L.-C.; Xue, C.-H.; Liu, B.-Y.; Guo, X.-J.; Wang, J.-H.; Deng, F.-Q. Scalable Superhydrophobic Flexible Nanofiber Film for Passive Daytime Radiative Cooling. *ACS Appl. Polym. Mater.* **2022**, *4*, 3343–3351.

(39) Solar resource maps of world: global horizontal irradiation. https://solargis.com/maps-and-gis-data/download/world (accessed 2024-03-15).

(40) Deru, M.; Field, K.; Studer, D.; Benne, K.; Griffith, B.; Torcellini, P.; Liu, B.; Halverson, M.; Winiarski, D.; Rosenberg, M.; Yazdanian, M.; Huang, J.; Crawley, D. U.S. Department of Energy commercial reference building models of the national building stock, National Renewable Energy Laboratory, Golden, CO, 2011; Report No. NREL/TP-5500–46861.

(41) Jia, Y.; Liu, D.; Chen, D.; Jin, Y.; Chen, C.; Tao, J.; Cheng, H.; Zhou, S.; Cheng, B.; Wang, X.; Meng, Z.; Liu, T. Transparent Dynamic Infrared Emissivity Regulators. *Nat. Commun.* **2023***, 14,* 5087.

(42) Beck, H. E.; Zimmermann, N. E.; McVicar, T. R.; Vergopolan, N.; Berg, A.; Wood, E. F. Present and future Köppen-Geiger climate classification maps at 1-km resolution. *Sci. Data*, **2018**, *5*, 180214.

(43) Peng, Y.; Fan, L.; Jin, W.; Ye, Y.; Huang, Z.; Zhai, S.; Luo, X.; Ma, Y.; Tang, J.; Zhou, J.; Greenburg, L. C.; Majumdar, A.; Fan, S.; Cui, Y. Coloured Low-Emissivity Films for Building Envelopes for Year-Round Energy Savings. *Nat. Sustain.* **2021**, *5*, 339–347.

(44) Galib, R. H.; Tian, Y.; Lei, Y.; Dang, S.; Li, X.; Yudhanto, A.; Lubineau, G.; Gan, Q. Atmospheric-Moisture-Induced Polyacrylate Hydrogels for Hybrid Passive Cooling. *Nat. Commun.* **2023**, *14*, 6707.